

Adams Bashforth Moulton Solver for Inversion and Editing in Rectified Flow

Yongjia Ma¹ Donglin Di¹ Xuan Liu² Xiaokai Chen²
 Lei Fan³ Wei Chen¹ Tonghua Su²

¹Li Auto ²Harbin Institute of Technology ³University of New South Wales

Abstract

Rectified flow models have achieved remarkable performance in image and video generation tasks. However, existing numerical solvers face a trade-off between fast sampling and high-accuracy solutions, limiting their effectiveness in downstream applications such as reconstruction and editing. To address this challenge, we propose leveraging the Adams-Bashforth-Moulton (ABM) predictor-corrector method to enhance the accuracy of ODE solving in rectified flow models. Specifically, we introduce ABM-Solver, which integrates a multi-step predictor-corrector approach to reduce local truncation errors and employs Adaptive Step Size Adjustment to improve sampling speed. Furthermore, to effectively preserve non-edited regions while facilitating semantic modifications, we introduce a Mask Guided Feature Injection module. We estimate self-similarity to generate a spatial mask that differentiates preserved regions from those available for editing. Extensive experiments on multiple high-resolution image datasets validate that ABM-Solver significantly improves inversion precision and editing quality, outperforming existing solvers without requiring additional training or optimization.

1. Introduction

Diffusion models have emerged as the dominant paradigm for high-fidelity image and video generation [13, 16, 31, 34]. These models learn to reverse the forward process of transforming data into noise, effectively capturing high-dimensional perceptual data structures. Early approaches, e.g., DDPM [16], rely on stochastic differential equations (SDEs) to iteratively denoise samples, requiring extensive computation during generation. To enhance efficiency and accuracy, recent advancements in flow matching [23, 24] have demonstrated superior generative performance with faster training and inference [13, 20]. This shift is attributed to architectures like DiT [29], gradually replacing the UNet backbone [32] and reformulating SDEs as ordinary differ-

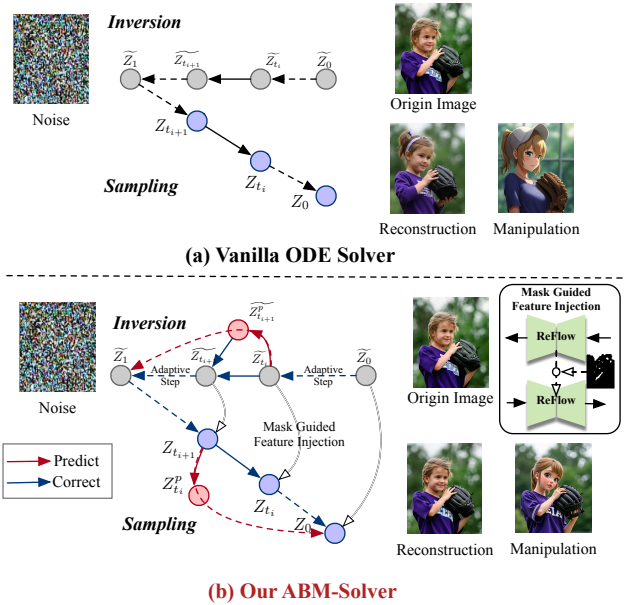


Figure 1. Comparison of Vanilla ODE Solver and Our ABM-Solver. (a) **Vanilla ODE Solver**: Conventional numerical integration accumulates approximation errors, compromising inversion accuracy and editing fidelity. (b) **Our ABM-Solver**: By integrating a second-order ABM predictor-corrector framework, the Adaptive Step Size Adjustment, and Mask Guided Feature Injection, our method significantly reduces errors and achieves superior inversion and semantic editing performance.

ential equations (ODEs). By transitioning from stochastic to deterministic formulations, these models directly learn smooth velocity fields, enabling faster and more stable sampling [19, 21, 39].

Building on earlier advancements, Rectified Flow (ReFlow) models optimize velocity trajectories by leveraging numerical solvers, such as the Euler method or high-order Taylor expansions to enforce near-linear transformations [1, 36]. These methods reduce cumulative errors and improve inversion quality. However, increasing the solver’s

order typically comes at the expense of computational efficiency; alternative approaches like the Midpoint Method [8], while potentially faster, can be overly sensitive to step-size selection and may suffer from stability issues. Consequently, the inversion process becomes progressively less accurate over extended integration horizons, which directly undermines the performance of downstream applications including reconstruction and editing.

To address discretization errors arising from fixed-step integration, we present the ABM-Solver, a linear multistep method that integrates a two-step predictor–corrector approach [11], with an adaptive step size adjustment mechanism to dynamically adjust step sizes driven by local truncation error estimates. During the first stage (*i.e.*, explicit prediction), the Adams–Bashforth method estimates the next state from a weighted sum of previously computed gradients, providing fast yet potentially coarse approximations. Subsequently, this is refined by the second stage (*i.e.*, implicit corrector) via the Adams–Moulton method, which incorporates newly evaluated gradients to reduce local errors and improve stability.

In addition to enhancing inversion precision and reconstruction accuracy, we thoroughly analyze the spatial consistency of attention values between the inversion and sampling stages. Specifically, we introduce a Mask Guided Feature Injection module that effectively supports a wide range of editing tasks while preserving the original content’s semantics. To achieve this, we estimate self-similarity to generate a spatial mask that differentiates between regions requiring preservation and those amenable to modification. This mask-guided fusion of attention features helps retain critical structural details in non-edited areas while enabling flexible semantic alterations where needed. Extensive theoretical analysis and empirical evaluations on multiple high-resolution image datasets demonstrate that our approach effectively balances computational efficiency and numerical precision, outperforming existing methods without requiring additional training or optimization costs. Our contributions are summarized as follows:

- We propose ABM-Solver, a training-free numerical solver that integrates the Adams–Bashforth–Moulton predictor–corrector method with Adaptive Step Size Adjustment, achieving second-order accuracy and reduced local truncation errors in Rectified Flow models without extra computational cost.
- We introduce a Mask Guided Feature Injection module, which leverages spatial consistency of attention values to generate masks for selectively fusing features, thereby preserving structural details while enabling semantically consistent editing.
- Extensive theoretical analysis and experiments on high-resolution image datasets demonstrate that our approach significantly improves inversion precision

and reconstruction accuracy, and supports diverse editing tasks, outperforming existing solvers without requiring extra training.

2. Related Work

Diffusion Inversion Diffusion inversion involves mapping a real image back into the latent noise space from which it can be reconstructed or manipulated, fundamental for tasks such as image reconstruction [2, 6, 22] and editing [3, 7, 9, 38]. Denoising Diffusion Implicit Models (DDIM) inversion [34] formulates the sampling process as an ODE and inverts it to recover the initial latent noise, but its reconstruction accuracy declines when applied to text-guided diffusion models with few denoising steps [14]. Null-text Inversion (NTI) [27] optimizes the null-text embedding during inversion for accurate reconstruction but requires per-image optimization, which is computationally intensive. NPI [26] replaces the null-text embedding with a negative prompt embedding to eliminate the need for optimization but sacrifices some reconstruction accuracy. Direct Inversion [12] incorporates inverted noises corresponding to each timestep to mitigate content leakage, but balancing efficiency and accuracy remains challenging. In rectified flow models, RF-Inversion [33] uses dynamic optimal control to improve inversion accuracy. RF-Solver [36] applies high-order Taylor expansions to reduce approximation errors in the ODEs of rectified flow. FireFlow [8] introduces a numerical solver that achieves second-order precision with the computational cost of a first-order solver. However, these methods either require increased computational resources or struggle to balance efficiency and precision in inversion accuracy.

Editing with Inversion Methods Editing with inversion methods [5, 10, 18] relies on accurate inversion techniques to manipulate images in the latent space. Prompt-to-Prompt editing [14] manipulates cross-attention maps to guide the editing process. MasaCtrl [4] incorporates mutual self-attention control for precise non-rigid editing. Plug-and-Play methods [35] substitute attention matrices in the denoising steps with those from the inversion of the source image, preserving structural details while enabling prompt-based edits. Despite these advancements, existing methods [25, 34, 40] either require many inversion steps, leading to increased computational time or struggle to balance editing flexibility with preservation of the source image’s content. By addressing these limitations, our proposed ABM-Solver provides a more accurate inversion with fewer steps due to its higher-order accuracy and theoretical convergence properties, enhancing the effectiveness of editing methods with minimal computational costs.

3. Preliminaries

In this section, we provide the necessary background on Rectified Flow models and their mathematical formulations, which form the foundation of our proposed method.

Rectified Flow models [24] offer a principled approach for modeling transformations between two distributions: a source distribution π_0 and a target distribution π_1 . Given samples $\mathbf{Z}_0 \sim \pi_0$ and $\mathbf{Z}_1 \sim \pi_1$, the goal is to learn a transformation that maps \mathbf{Z}_0 to \mathbf{Z}_1 through a continuous flow over time $t \in [0, 1]$. The transformation is represented by an ordinary differential equation (ODE):

$$\frac{d\mathbf{Z}(t)}{dt} = \mathbf{v}_\theta(\mathbf{Z}(t), t), \quad (1)$$

where $\mathbf{Z}(t) \in \mathbb{R}^d$ is the state at time t , and $\mathbf{v}_\theta : \mathbb{R}^d \times [0, 1] \rightarrow \mathbb{R}^d$ is the velocity field parameterized by neural network parameters θ . The velocity field \mathbf{v}_θ governs the flow of the latent variables over time, directing the transformation from the source to the target distribution.

3.1. Forward Process

The forward process seeks to transform samples from the source distribution π_0 to match the target distribution π_1 . A direct parameterization of the trajectory is given by linear interpolation:

$$\mathbf{Z}_t = (1 - t)\mathbf{Z}_0 + t\mathbf{Z}_1, \quad t \in [0, 1], \quad (2)$$

It satisfies the non-causal ODE:

$$\frac{d\mathbf{Z}_t}{dt} = \mathbf{Z}_1 - \mathbf{Z}_0, \quad (3)$$

However, this formulation requires knowledge of \mathbf{Z}_1 at all intermediate time steps, which is impractical for simulation. To overcome this, a velocity field $\mathbf{v}_\theta(\mathbf{Z}(t), t)$ is learned to approximate the linear interpolation direction without requiring \mathbf{Z}_1 during the forward process. The causalized forward ODE becomes:

$$\frac{d\mathbf{Z}(t)}{dt} = \mathbf{v}_\theta(\mathbf{Z}(t), t), \quad (4)$$

where $\mathbf{Z}(0) \sim \pi_0$ is initialized from the source distribution. The velocity field is trained by minimizing the following objective:

$$\min_{\theta} \mathbb{E}_{\mathbf{Z}_0, \mathbf{Z}_1} \left[\int_0^1 \|\mathbf{Z}_1 - \mathbf{Z}_0 - \mathbf{v}_\theta(\mathbf{Z}_t, t)\|_2^2 dt \right], \quad (5)$$

where \mathbf{Z}_t is the linear interpolation between \mathbf{Z}_0 and \mathbf{Z}_1 as in Equation (2). This objective ensures that the velocity field \mathbf{v}_θ approximates the transformation from \mathbf{Z}_0 to \mathbf{Z}_1 over time, by matching the trajectory generated by linear interpolation.

3.2. Reverse Process

To generate samples from π_1 , the learned flow is reversed. Starting from $\mathbf{Z}(1) \sim \pi_1$, the reverse ODE is defined as:

$$\frac{d\mathbf{Z}(t)}{dt} = -\mathbf{v}_\theta(\mathbf{Z}(t), t), \quad t \in [1, 0], \quad (6)$$

It effectively transforms samples from π_1 to π_0 by “undoing” the forward transformations. In this reverse process, the learned velocity field \mathbf{v}_θ is used with the opposite sign to recover the original distribution π_0 from samples in π_1 .

4. Methods

4.1. Adams-Bashforth-Moulton Solver

RF-based models are capable of generating high-quality images and videos. However, when applied to reconstruction and editing tasks, recent studies have found that approximations in solving the corrected flow ODE lead to significant error accumulation at each time step [8, 36]. Therefore, by improving the numerical integration process to obtain a more accurate solution to the ODE, we aim to reduce error accumulation, thereby enhancing the performance of corrected flow models in inversion and editing tasks.

Based on this analysis, we first carefully examine the differential form of the corrected flow: $d\mathbf{Z}(t) = -\mathbf{v}_\theta(\mathbf{Z}(t), t) dt$. During the sampling process, this ordinary differential equation (ODE) is discretized. Given the initial value \mathbf{Z}_{t_i} , the ODE can be accurately represented using the variant of constant method:

$$\mathbf{Z}_{t_{i-1}} = \mathbf{Z}_{t_i} + \int_{t_i}^{t_{i-1}} \mathbf{v}_\theta(\mathbf{Z}(\tau), \tau) d\tau, \quad (7)$$

where $\mathbf{Z}(\tau)$ denotes the evolving latent state (*e.g.*, an image tensor) and \mathbf{v}_θ is a neural-network-based velocity field designed for mapping between noise and real data distributions via a straight-line flow. A multi-step method approximates the integral by interpolating or extrapolating the function $\mathbf{v}_\theta(\mathbf{Z}(t_j), t_j)$ at several previous time points t_j .

4.1.1. Predictor Step: Adams-Bashforth Method

In the Adams-Bashforth method, the integral in Equation (7) is approximated by an explicit polynomial extrapolation based on previously computed evaluations of the velocity field at earlier time steps. The main idea behind this method is to use the velocity values at several previous time points to predict the future state of the system.

Specifically, for a given time step t_i and step size $h = t_{i-1} - t_i$, the two-step Adams-Bashforth method approximates the integral as:

$$\int_{t_i}^{t_{i-1}} \mathbf{v}_\theta(\mathbf{Z}(t), t) dt \approx h_i \sum_{j=0}^{p-1} \beta_j \mathbf{v}_\theta(\mathbf{Z}_{t_{i+j}}, t_{i+j}), \quad (8)$$

where β_j are the coefficients for the extrapolation, and the sum involves velocity field values at the previous time steps

t_{i+j} . The method relies on an explicit prediction from the previous steps, where the velocity field values at these steps guide the estimation of the integral over the current interval.

Once the integral approximation is computed, the predictor step computes an initial estimate for the system state at the next time step t_{i-1} . This is achieved by adding the computed approximation to the current state \mathbf{Z}_{t_i} :

$$\mathbf{Z}_{t_{i-1}}^{(p)} = \mathbf{Z}_{t_i} + \frac{h_i}{2} [3 \mathbf{v}_\theta(\mathbf{Z}_{t_i}, t_i) - \mathbf{v}_\theta(\mathbf{Z}_{t_{i+1}}, t_{i+1})], \quad (9)$$

This equation provides the prediction $\mathbf{Z}_{t_{i-1}}^{(p)}$ of the system state at the next time step, based on the previous evaluations of the velocity field. Since the Adams-Bashforth method is explicit, it is straightforward to compute and can be parallelized, making it computationally efficient.

4.1.2. Corrector Step: Adams-Moulton Method

Once the predictor step provides an estimate $\mathbf{Z}_{t_{i-1}}^{(p)}$ of the system state at t_{i-1} , the Adams-Moulton method is applied to refine this estimate through implicit integration. The corrector step improves the prediction by incorporating additional information, particularly the velocity field at t_{i-1} , which was not included in the explicit prediction.

The Adams-Moulton method employs the following integral approximation, which considers the velocity field at the predicted state t_{i-1} along with previous states:

$$\int_{t_i}^{t_{i-1}} \mathbf{v}_\theta(\mathbf{Z}(t), t) dt \approx h_i [\alpha_0 \mathbf{v}_\theta(\mathbf{Z}_{t_{i-1}}^{(p)}, t_{i-1}) + \sum_{j=0}^{p-1} \alpha_{j+1} \mathbf{v}_\theta(\mathbf{Z}_{t_{i+j}}, t_{i+j})], \quad (10)$$

where α_j are the coefficients for the extrapolation. This equation refines the integral estimate by including the velocity field evaluation at t_{i-1} , which was initially ignored in the Adams-Bashforth step.

The corrected estimate of $\mathbf{Z}_{t_{i-1}}$ is then computed by updating the state based on the refined approximation:

$$\mathbf{Z}_{t_{i-1}} = \mathbf{Z}_{t_i} + \frac{h_i}{2} [\mathbf{v}_\theta(\mathbf{Z}_{t_{i-1}}^{(p)}, t_{i-1}) + \mathbf{v}_\theta(\mathbf{Z}_{t_i}, t_i)], \quad (11)$$

This correction step improves the prediction obtained from the Adams-Bashforth method, leading to a more accurate estimate of the system's state at the next time step. The key advantage of the Adams-Moulton method is that it considers the velocity field at the predicted state, which helps improve the stability and accuracy of the solution.

To balance computational efficiency and accuracy, we employ the second-order Adams-Bashforth-Moulton (ABM) method. This method combines the explicit Adams-Bashforth method with the implicit Adams-Moulton method to provide an efficient and accurate numerical integration. The procedure consists of two steps: first,

Algorithm 1: ABM-Solver for Rectified Flow ODE (Second-Order)

Input: origin latent \mathbf{Z} , time steps $\{t_N, t_{N-1}, \dots, t_0\}$
Initialize:
 $\mathbf{k}_1 = \mathbf{v}_\theta(\mathbf{Z}_{t_N}, t_N)$
 $\mathbf{k}_2 = \mathbf{v}_\theta(\mathbf{Z}_{t_N} + h\mathbf{k}_1, t_N + h)$
 $\mathbf{Z}_{t_{N-1}} = \mathbf{Z}_{t_N} + \frac{h}{2}(\mathbf{k}_1 + \mathbf{k}_2)$
for each timestep t_i from t_N to t_0 **do**
 Predict: \rightarrow Equation (9)
 Correct: \rightarrow performing Equation (11)
end for
Output \mathbf{Z}_{t_N}

an explicit prediction step using the second-order Adams-Bashforth method, followed by an implicit correction step using the second-order Adams-Moulton method.

4.1.3. Second-Order Runge-Kutta Initialization

The ABM method requires starting values from previous time steps. To obtain accurate initial values, we use the second-order Runge-Kutta (RK2) method for the first step:

$$\mathbf{Z}_{t_{N-1}} = \mathbf{Z}_{t_N} + \frac{h}{2} (\mathbf{v}_\theta(\mathbf{Z}_{t_N}, t_N) + \mathbf{v}_\theta(\mathbf{Z}_{t_N} + h\mathbf{v}_\theta(\mathbf{Z}_{t_N}, t_N), t_N + h)), \quad (12)$$

The complete algorithm for the ABM-Solver is presented in Algorithm 1. This method significantly improves precision in reconstruction and editing tasks, particularly when using fewer timesteps.

Furthermore, consider an ODE $\frac{d\mathbf{Z}}{dt} = v_\theta(\mathbf{Z}, t)$ with solution $\mathbf{Z}(t)$. Let Δt be the step size, and assume v_θ is sufficiently smooth in both \mathbf{Z} and t . For a single step from t to $t + \Delta t$, the two-step Adams-Bashforth-Moulton solver has a local truncation error of $\mathcal{O}(\Delta t^3)$. More precisely, if $\mathbf{Z}(t)$ is assumed exact at previous steps, then the difference between the true solution $\mathbf{Z}(t + \Delta t)$ and the ABM numerical update $\mathbf{Z}_{t+\Delta t}$ is on the order of Δt^3 . Consequently, over the entire interval $[0, T]$, the global error typically accumulates to $\mathcal{O}(\Delta t^2)$, improving upon the $\mathcal{O}(\Delta t)$ global error of a first-order (Euler) method:

$$\begin{cases} \underbrace{\|\mathbf{Z}_{t+\Delta t} - \mathbf{Z}_{t+\Delta t}^{(\text{ABM})}\|}_{\text{local error}} \leq C(\Delta t)^3, \\ \underbrace{\|\mathbf{Z}_t - \mathbf{Z}_t^{(\text{ABM})}\|}_{\text{global error}} \leq C'(\Delta t)^2, \end{cases} \quad (13)$$

Analogous to the analysis in [8], these error bounds hinge on v_θ being Lipschitz-continuous in \mathbf{Z} and sufficiently smooth in t . Under these conditions, the predictor step (Adams-Bashforth) and corrector step (Adams-Moulton) both incur only $\mathcal{O}(\Delta t^3)$ local defects, leading to the overall $\mathcal{O}(\Delta t^2)$ global accuracy. Thus, although high-order

schemes may require additional NFEs when naively implemented, methods, that re-use previously computed velocities or adopt predictor-corrector updates (*e.g.*, ABM-Solver), can retain second-order performance without doubling the per-step cost. This allows the solver to match the runtime of a first-order approach while delivering higher fidelity results.

4.2. Adaptive Step Size Adjustment

To balance numerical accuracy and computational efficiency, we develop an Adaptive Step Size Adjustment strategy for the ABM solver. The key idea is to dynamically adjust the integration step size based on local truncation error estimates, allowing larger steps in regions where the solution varies smoothly and smaller steps near high-curvature regions.

Let $h_i = t_{i-1} - t_i$ denote the current step size, and define the local error estimate ϵ_i as the discrepancy between the predictor and corrector steps:

$$E_{i-1} = \left\| \mathbf{Z}_{t_{i-1}}^{(p)} - \mathbf{Z}_{t_{i-1}} \right\|_2, \quad (14)$$

where $\mathbf{Z}_{t_{i-1}}^{(p)}$ and $\mathbf{Z}_{t_{i-1}}$ are the predicted and corrected states from Equation. (9) and (11), respectively. The step size adaptation follows the error-controlled update rule:

$$h_{i-1} = h_i \times \left(\frac{\epsilon}{E_{i-1}} \right)^{\frac{1}{p+1}}, \quad (15)$$

where ϵ is the error tolerance, and $p = 2$ represents the method’s order. This adaptation mechanism automatically reduces step sizes when local errors exceed the tolerance ϵ while expanding steps in smooth regions where errors remain below the threshold. The default setting of ϵ is 0.1.

It maintains numerical stability by preventing error accumulation through local error monitoring and improves computational efficiency. This dynamic balance makes the method particularly suitable for inversion and editing tasks where both precision and efficiency are critical.

4.3. Mask Guided Feature Injection

In the context of diffusion model-based image and video editing tasks, achieving a balance between semantic editing and preserving the structural integrity of the source image is of paramount importance. Notably, in the DiT model, the Attention Values (V) play a significant role in influencing the editing outcomes. To this end, by meticulously analyzing the spatial consistencies between the inversion and sampling processes with respect to the attention values, the regions amenable to editing can be more precisely identified, thereby striking an optimal balance between editability and fidelity to the input image.

To reconcile the preservation of structural information with semantic editing, we conduct an in-depth analysis of

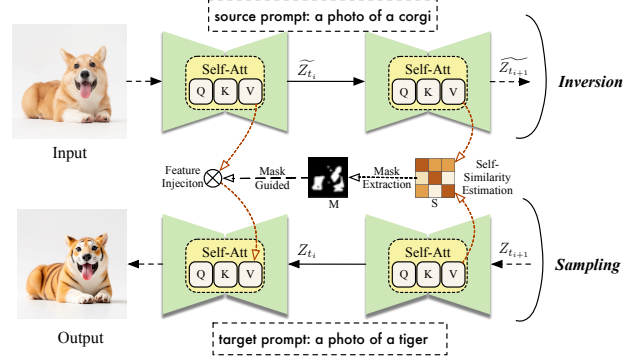


Figure 2. Mask Guided Feature Injection.

the spatial consistencies between the attention values in the inversion and sampling processes. For aligned timesteps t_i , we define:

$$\tilde{V}_{t_i} = \mathcal{F}(\tilde{Z}_{t_i}, t_i), \quad V_{t_i} = \mathcal{F}(Z_{t_i}, t_i), \quad (16)$$

where \mathcal{F} represents the function mapping the latent variables and timestep to the corresponding attention values.

Self Similarity Mask Estimation. To quantitatively measure the similarity between the Attention Values in the inversion and sampling processes, we compute the pixel-wise cosine similarity \mathbf{S}_{t_i} . Cosine similarity is a commonly employed metric for gauging the directional alignment between two vectors. In our context, calculating the cosine similarity between \tilde{V}_{t_i} and V_{t_i} determines the degree of similarity in the attention values at the same timestep across different processes. The computation is given by:

$$\mathbf{S}_{t_i} = \frac{\tilde{V}_{t_i} \cdot V_{t_i}}{\|\tilde{V}_{t_i}\| \|V_{t_i}\|}, \quad (17)$$

We generate a spatial mask \mathbf{M} using a threshold τ :

$$\mathbf{M} = \begin{cases} 1 & \mathbf{S}_{t_i} \geq \tau \\ 0 & \text{otherwise,} \end{cases} \quad (18)$$

If the cosine similarity \mathbf{S} at a pixel location meets or exceeds the threshold τ , the corresponding value in the spatial mask \mathbf{M} is set to 1, signifying that the attention values in that region exhibit strong consistency between the inversion and sampling processes and should be retained. Conversely, if \mathbf{S} is below τ , the corresponding value in \mathbf{M} is set to 0, indicating that the region may be subject to editing. The default threshold τ is set to 0.2.

Mask Guided Feature Fusion. Once the spatial mask \mathbf{M} is obtained, it is used to merge the attention values, ensuring the preservation of crucial features. Specifically, we adopt a mask-directed blending strategy to combine $\tilde{V}_{t_{i-1}}$ and $V_{t_{i-1}}$, formulated as:

$$V_{t_{i-1}} = \mathbf{M} \odot \tilde{V}_{t_{i-1}} + (1 - \mathbf{M}) \odot V_{t_{i-1}}, \quad (19)$$

Table 1. Comparison of our ABM-Solver approach with other image editing methods on the PIE-Bench. Metrics include background preservation (measured by PSNR and SSIM), structural consistency (measured by distance), and CLIP similarity for both the whole and edited images. Additionally, the number of steps and function evaluations (NFE) are provided to reflect the efficiency of each method.

Method	Model	Structure	Background Preservation		CLIP Similarity \uparrow		Steps	NFE \downarrow
		Distance \downarrow	PSNR \uparrow	SSIM \uparrow	Whole	Edited		
Prompt2Prompt [14]	Diffusion	0.0694	17.87	0.7114	25.01	22.44	50	100
Pix2Pix-Zero [28]	Diffusion	0.0617	20.44	0.7467	22.80	20.54	50	100
MasaCtrl [4]	Diffusion	0.0284	22.17	0.7967	23.96	21.16	50	100
PnP [17]	Diffusion	0.0282	22.28	0.7905	25.41	22.55	50	100
PnP-Inv. [12]	Diffusion	0.0243	22.46	0.7968	25.41	22.62	50	100
RF-Inversion [33]	ReFlow	0.0406	20.82	0.7192	25.20	22.11	28	56
RF-Solver [36]	ReFlow	0.0311	22.90	0.8190	26.00	22.88	15	60
FireFlow [8]	ReFlow	0.0283	23.28	0.8282	25.98	22.94	15	32
Ours	ReFlow	0.0207	24.60	0.8305	27.31	22.97	15	40-60

Table 2. Quantitative comparison of inversion and reconstruction performance. ReFlow-Inv., RF-Solver, FireFlow, and ABM-Solver are based on the FLUX-dev model. The NFE includes both inversion and reconstruction function evaluations, and computational costs (steps) are kept comparable across methods.

	Steps	NFE \downarrow	LPIPS \downarrow	SSIM \uparrow	PSNR \uparrow
DDIM-Inv.	50	100	0.2342	0.5872	19.72
ReFlow-Inv.	30	60	0.5044	0.5632	16.57
RF-Solver	20	80	0.1653	0.5903	20.16
FireFlow	20	42	0.1359	0.6172	20.37
Ours	15	40-60	0.1309	<u>0.6004</u>	20.66

Table 3. Ablation Study of Mask Guided Feature Injection in ABM-Solver

Methods	Distance \downarrow	PSNR \uparrow	SSIM \uparrow	CLIP (Whole) \uparrow	CLIP (Edit) \uparrow
w/o MGFI	0.0274	23.08	0.8142	24.98	22.01
- w/o Mask	0.0271	23.65	0.8273	25.39	22.42
Ours	0.0207	24.60	0.8305	27.31	22.97

where \odot stands for element-wise multiplication. This strategy leverages the broader contextual estimation provided by the mask from the prior time step to mitigate localization errors in attention fusion. Consequently, during the editing procedure, we can successfully maintain the structural integrity of the source image while also fulfilling the requirements of semantic editing. Through this meticulous manipulation and examination of the Attention Values in both inversion and sampling phases, we gain enhanced control over the model’s editing conduct. This allows us to preserve the original image structure and achieve high-caliber semantic editing, striking an excellent balance between editability and fidelity.



Figure 3. Qualitative results of image reconstruction with our ABM-Solver, FireFlow, RF-Solver, and ReFlow-Inv. The results demonstrate that ABM-Solver provides superior structural consistency and detail preservation compared to other methods.

5. Experiment

5.1. Setup

Baselines This section compares Our ABM-solver with DM inversion-based editing methods such as Prompt-to-Prompt [14], MasaCtrl [4], Pix2Pixzero [28], Plug-and-Play [35], and DirectInversion [12]. We also consider the recent RF inversion methods, such as RF-Inversion [33], RF-Solver [36] and FireFlow [8].

Metric To comprehensively assess different methods, we conduct evaluations from three key perspectives: generation quality, preservation quality, and text-guided quality. Firstly, to evaluate the preservation quality of non-edited regions, a series of metrics come into play. These include the Learned Perceptual Image Patch Similarity (LPIPS) [41], which measures certain perceptual similarities; the Structural Similarity Index Measure (SSIM) [37] that focuses on

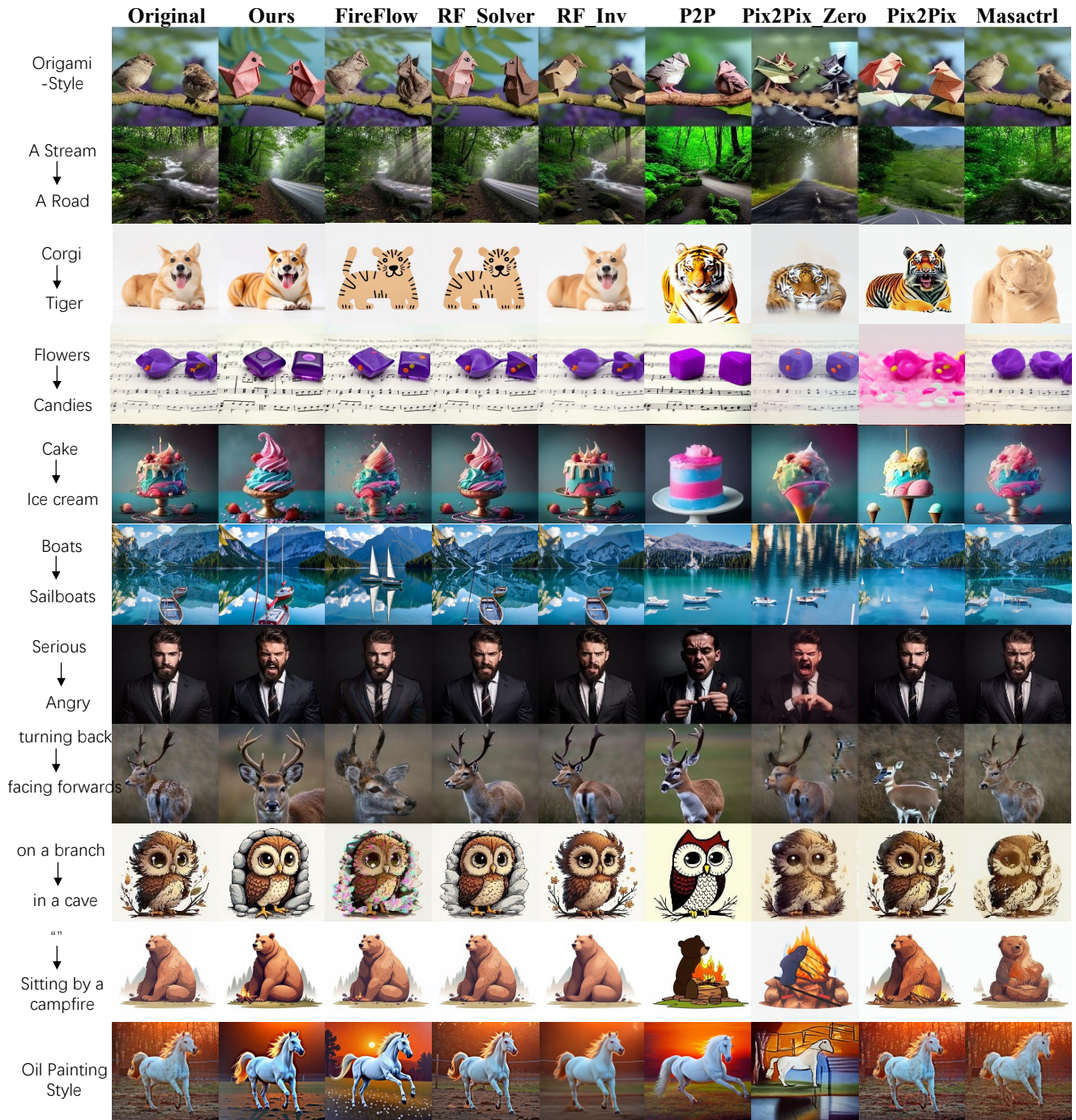


Figure 4. Qualitative comparison of image editing results across different methods. Our ABM-Solver demonstrates superior performance, delivering better results in both content preservation and the accuracy of applied edits, particularly in more complex tasks such as object substitution, background editing, and style transfer.

structural likeness; the Peak Signal-to-Noise Ratio (PSNR) for quantifying signal and noise relationships; and also the structural distance [15]. Lastly, in order to figure out the similarity between the generated image and the guiding text, a CLIP model [30] is utilized.

5.2. Image Editing

We evaluate the ABM-Solver’s image editing performance through tasks such as subject replacement, geometry changes, object addition, and global modifications. For object substitution and insertion, it is essential to preserve the background, while global edits like style transfer re-

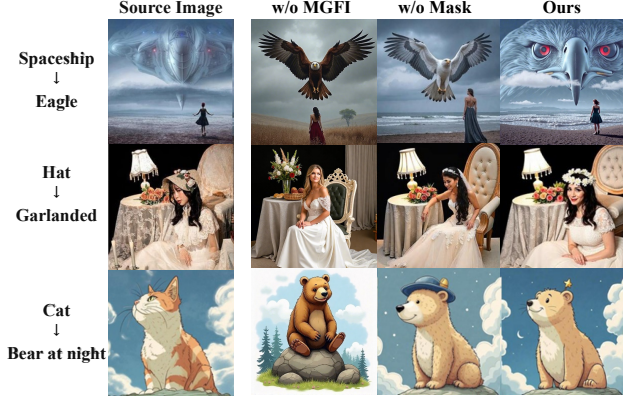


Figure 5. Ablation Results of Mask Guided Feature Injection module in our ABM solver.

quire maintaining the overall structure and composition of the original image. ABM-Solver meets these objectives, delivering high-quality results and preserving the integrity of the original content.

Quantitative Results To evaluate image editing capabilities, we utilize the PIE-Bench dataset [17]. This dataset includes 700 images and encompasses 10 distinct editing tasks. As shown in Table 1, ABM-Solver consistently outperforms other methods, demonstrating its ability to maintain high preservation quality while aligning with the intended modifications. ABM-Solver achieves efficient, high-quality edits with fewer steps by combining the multi-step ABM predictor-corrector method, which balances accuracy and speed. The Mask Guided Feature Injection module further enhances editing by preserving non-edited regions while allowing effective semantic changes. Experiments on high-resolution image datasets confirm that ABM-Solver improves inversion precision and editing quality, outperforming existing solvers without additional training. Overall, it offers an optimal balance between accuracy and computational efficiency, making it highly effective for both precise and efficient editing tasks.

Quantitative Results The visual results of image editing using the ABM-Solver are presented in Figure 4. Our approach effectively balances content preservation with the accuracy of applied edits, excelling in appearance editing, style editing, and geometry editing. In appearance editing tasks, our ABM-Solver outperforms other methods. It can precisely modify specific elements while maintaining the integrity of surrounding areas. In contrast, methods like P2P, Pix2Pix-Zero, MasaCtrl, and PnP often introduce visual inconsistencies in unchanged regions. Regarding style editing, ABM-Solver smoothly applies the desired style changes, such as converting to “Origami-Style” or “Oil Painting Style”, while preserving the original image’s overall structure. Others may disrupt the structure during the process. For geometry editing that requires keeping the ob-

ject’s identity, ABM-Solver strikes a better balance. Although methods like RF-Solver and FireFlow still have minor issues in unmodified regions. Meanwhile, Diffusion-based methods struggle to fully implement intended geometric changes. Overall, ABM-Solver consistently delivers more accurate results across diverse editing prompts, making it a more reliable option for image editing, excelling in both content preservation and high-quality edits.

5.3. Inversion and Reconstruction

We conduct experiments on inversion and reconstruction tasks, comparing our ABM-Solver with the vanilla RF sampler, RF Solver, FireFlow and DDIM Inversion.

Quantitative Results The quantitative results, shown in Table 2, demonstrate that ABM-Solver outperforms the other methods across all four metrics. Despite slightly lower performance in one metric, our approach requires fewer steps to achieve comparable or superior image reconstruction quality, illustrating its efficiency and effectiveness. While FireFlow achieves slightly better SSIM scores, ABM-Solver requires only 15 steps compared to FireFlow’s 20, demonstrating its superior computational efficiency without sacrificing reconstruction quality.

Performance Analysis ABM-Solver significantly reduces errors in solving the RF ODE, enhancing the accuracy of image reconstruction. As illustrated in Fig 3, when the standard rectified flow approach is used, the reconstructed images exhibit notable deviations from the original, causing undesirable alterations in subject appearance. In contrast, ABM-Solver minimizes these deviations, providing higher fidelity reconstructions with fewer steps.

5.4. Ablation Study

In this section, we conduct ablation studies to evaluate the effectiveness of the Mask Guided Feature Injection (MGFI) module in our proposed ABM-Solver. We investigate the impact of different components of our method, including the inclusion of the mask and the feature Injection strategy. This analysis helps quantify the contribution of each component to the overall performance editing quality. As shown in Table 3, the quantitative results clearly demonstrate the significant impact of the MGFI module. MGFI effectively improves editing quality and maintains background consistency. The qualitative results, presented in Figure 5, further highlight that without the MGFI module, the edited images fail to maintain consistency between the original and edited content. Additionally, removing the spatial mask leads to noticeable deviations in certain fine details.

6. Conclusion

In this work, we present ABM-Solver, a training-free, high-order numerical solver that leverages the Adams–Bashforth–Moulton predictor–corrector approach in conjunction with Adaptive Step Size Adjustment. By dy-

namically adjusting the integration steps, ABM-Solver effectively mitigates the accumulation of discretization errors while maintaining computational efficiency. Furthermore, by coupling it with our proposed Mask Guided Feature Injection module, ABM-Solver achieves precise inversion and high-fidelity, semantically guided editing. Extensive experiments on high-resolution datasets demonstrate that ABM-Solver not only significantly improves inversion accuracy but also surpasses existing solvers in both speed and fidelity. These advancements underscore the potential of rectified flow models for reliable, high-quality content generation and editing, paving the way for broader adoption across computational media and related fields.

References

- [1] Omri Avrahami, Or Patashnik, Ohad Fried, Egor Nemchinov, Kfir Aberman, Dani Lischinski, and Daniel Cohen-Or. Stable flow: Vital layers for training-free image editing. *arXiv preprint arXiv:2411.14430*, 2024. 1
- [2] Manuel Brack, Felix Friedrich, Katharina Kornmeier, Linoy Tsaban, Patrick Schramowski, Kristian Kersting, and Apolinário Passos. Ledits++: Limitless image editing using text-to-image models, 2024. 2
- [3] Tim Brooks, Aleksander Holynski, and Alexei A. Efros. Instructpix2pix: Learning to follow image editing instructions, 2023. 2
- [4] Mingdeng Cao, Xintao Wang, Zhongang Qi, Ying Shan, Xiaohu Qie, and Yinqiang Zheng. Masactrl: Tuning-free mutual self-attention control for consistent image synthesis and editing. In *Proceedings of the IEEE/CVF International Conference on Computer Vision*, pages 22560–22570, 2023. 2, 6
- [5] Weifeng Chen, Yatai Ji, Jie Wu, Hefeng Wu, Pan Xie, Jishi Li, Xin Xia, Xuefeng Xiao, and Liang Lin. Control-a-video: Controllable text-to-video diffusion models with motion prior and reward feedback learning, 2024. 2
- [6] Hansam Cho, Jonghyun Lee, Seoung Bum Kim, Tae-Hyun Oh, and Yonghyun Jeong. Noise map guidance: Inversion with spatial context for real image editing, 2024. 2
- [7] Guillaume Couairon, Jakob Verbeek, Holger Schwenk, and Matthieu Cord. Diffedit: Diffusion-based semantic image editing with mask guidance, 2022. 2
- [8] Yingying Deng, Xiangyu He, Changwang Mei, Peisong Wang, and Fan Tang. Fireflow: Fast inversion of rectified flow for image semantic editing. *arXiv preprint arXiv:2412.07517*, 2024. 2, 3, 4, 6
- [9] Gilad Deutch, Rinon Gal, Daniel Garibi, Or Patashnik, and Daniel Cohen-Or. Turboedit: Text-based image editing using few-step diffusion models, 2024. 2
- [10] Xiaoyue Duan, Shuhao Cui, Guoliang Kang, Baochang Zhang, Zhengcong Fei, Mingyuan Fan, and Junshi Huang. Tuning-free inversion-enhanced control for consistent image editing, 2023. 2
- [11] Dale R Durran. The third-order adams-bashforth method: An attractive alternative to leapfrog time differencing. *Monthly weather review*, 119(3):702–720, 1991. 2
- [12] Adham Elarabawy, Harish Kamath, and Samuel Denton. Direct inversion: Optimization-free text-driven real image editing with diffusion models. *arXiv preprint arXiv:2211.07825*, 2022. 2, 6
- [13] Patrick Esser, Sumith Kulal, Andreas Blattmann, Rahim Entezari, Jonas Müller, Harry Saini, Yam Levi, Dominik Lorenz, Axel Sauer, Frederic Boesel, et al. Scaling rectified flow transformers for high-resolution image synthesis. In *Forty-first International Conference on Machine Learning*, 2024. 1
- [14] Amir Hertz, Ron Mokady, Jay Tenenbaum, Kfir Aberman, Yael Pritch, and Daniel Cohen-Or. Prompt-to-prompt image editing with cross attention control. *arXiv preprint arXiv:2208.01626*, 2022. 2, 6
- [15] Martin Heusel, Hubert Ramsauer, Thomas Unterthiner, Bernhard Nessler, and Sepp Hochreiter. Gans trained by a two time-scale update rule converge to a local nash equilibrium. *Advances in neural information processing systems*, 30, 2017. 7
- [16] Jonathan Ho, Ajay Jain, and Pieter Abbeel. Denoising diffusion probabilistic models. *Advances in neural information processing systems*, 33:6840–6851, 2020. 1
- [17] Xuan Ju, Ailing Zeng, Yuxuan Bian, Shaoteng Liu, and Qiang Xu. Pnp inversion: Boosting diffusion-based editing with 3 lines of code. In *The Twelfth International Conference on Learning Representations*, 2024. 6, 8
- [18] Ozgur Kara, Bariscan Kurtkaya, Hidir Yesiltepe, James M. Rehg, and Pinar Yanardag. Rave: Randomized noise shuffling for fast and consistent video editing with diffusion models, 2023. 2
- [19] Beomsu Kim, Yu-Guan Hsieh, Michal Klein, Marco Cuturi, Jong Chul Ye, Bahjat Kawar, and James Thornton. Simple reflow: Improved techniques for fast flow models. *arXiv preprint arXiv:2410.07815*, 2024. 1
- [20] Black Forest Labs. Flux. <https://github.com/black-forest-labs/flux>, 2023. 1
- [21] Sangyun Lee, Zinan Lin, and Giulia Fanti. Improving the training of rectified flows. *Advances in Neural Information Processing Systems*, 37:63082–63109, 2025. 1
- [22] Haonan Lin, Mengmeng Wang, Jiahao Wang, Wenbin An, Yan Chen, Yong Liu, Feng Tian, Guang Dai, Jingdong Wang, and Qianying Wang. Schedule your edit: A simple yet effective diffusion noise schedule for image editing, 2024. 2
- [23] Yaron Lipman, Ricky TQ Chen, Heli Ben-Hamu, Maximilian Nickel, and Matt Le. Flow matching for generative modeling. *arXiv preprint arXiv:2210.02747*, 2022. 1
- [24] Xingchao Liu, Chengyue Gong, and Qiang Liu. Flow straight and fast: Learning to generate and transfer data with rectified flow. *arXiv preprint arXiv:2209.03003*, 2022. 1, 3
- [25] Cheng Lu, Yuhao Zhou, Fan Bao, Jianfei Chen, Chongxuan Li, and Jun Zhu. Dpm-solver: A fast ode solver for diffusion probabilistic model sampling in around 10 steps, 2022. 2
- [26] Daiki Miyake, Akihiro Iohara, Yu Saito, and Toshiyuki Tanaka. Negative-prompt inversion: Fast image inversion for editing with text-guided diffusion models. *arXiv preprint arXiv:2305.16807*, 2023. 2

- [27] Ron Mokady, Amir Hertz, Kfir Aberman, Yael Pritch, and Daniel Cohen-Or. Null-text inversion for editing real images using guided diffusion models. In *Proceedings of the IEEE/CVF Conference on Computer Vision and Pattern Recognition*, pages 6038–6047, 2023. 2
- [28] Gaurav Parmar, Krishna Kumar Singh, Richard Zhang, Yijun Li, Jingwan Lu, and Jun-Yan Zhu. Zero-shot image-to-image translation. In *ACM SIGGRAPH 2023 Conference Proceedings*, pages 1–11, 2023. 6
- [29] William Peebles and Saining Xie. Scalable diffusion models with transformers. In *Proceedings of the IEEE/CVF International Conference on Computer Vision*, pages 4195–4205, 2023. 1
- [30] Alec Radford, Jong Wook Kim, Chris Hallacy, Aditya Ramesh, Gabriel Goh, Sandhini Agarwal, Girish Sastry, Amanda Askell, Pamela Mishkin, Jack Clark, et al. Learning transferable visual models from natural language supervision. In *International conference on machine learning*, pages 8748–8763. PMLR, 2021. 7
- [31] Aditya Ramesh, Prafulla Dhariwal, Alex Nichol, Casey Chu, and Mark Chen. Hierarchical text-conditional image generation with clip latents, 2022. 1
- [32] Robin Rombach, Andreas Blattmann, Dominik Lorenz, Patrick Esser, and Björn Ommer. High-resolution image synthesis with latent diffusion models. In *Proceedings of the IEEE/CVF conference on computer vision and pattern recognition*, pages 10684–10695, 2022. 1
- [33] Litu Rout, Yujia Chen, Nataniel Ruiz, Constantine Caramanis, Sanjay Shakkottai, and Wen-Sheng Chu. Semantic image inversion and editing using rectified stochastic differential equations. *arXiv preprint arXiv:2410.10792*, 2024. 2, 6
- [34] Jiaming Song, Chenlin Meng, and Stefano Ermon. Denoising diffusion implicit models. *arXiv preprint arXiv:2010.02502*, 2020. 1, 2
- [35] Narek Tumanyan, Michal Geyer, Shai Bagon, and Tali Dekel. Plug-and-play diffusion features for text-driven image-to-image translation. In *Proceedings of the IEEE/CVF Conference on Computer Vision and Pattern Recognition*, pages 1921–1930, 2023. 2, 6
- [36] Jiangshan Wang, Junfu Pu, Zhongang Qi, Jiayi Guo, Yue Ma, Nisha Huang, Yuxin Chen, Xiu Li, and Ying Shan. Taming rectified flow for inversion and editing. *arXiv preprint arXiv:2411.04746*, 2024. 1, 2, 3, 6
- [37] Zhou Wang, Alan C Bovik, Hamid R Sheikh, and Eero P Simoncelli. Image quality assessment: from error visibility to structural similarity. *IEEE transactions on image processing*, 13(4):600–612, 2004. 6
- [38] Sihan Xu, Yidong Huang, Jiayi Pan, Ziqiao Ma, and Joyce Chai. Inversion-free image editing with natural language, 2023. 2
- [39] Hanshu Yan, Xingchao Liu, Jiachun Pan, Jun Hao Liew, Qiang Liu, and Jiashi Feng. Perflow: Piecewise rectified flow as universal plug-and-play accelerator. *Advances in Neural Information Processing Systems*, 37:78630–78652, 2025. 1
- [40] Lvmin Zhang, Anyi Rao, and Maneesh Agrawala. Adding conditional control to text-to-image diffusion models, 2023. 2
- [41] Richard Zhang, Phillip Isola, Alexei A Efros, Eli Shechtman, and Oliver Wang. The unreasonable effectiveness of deep features as a perceptual metric. In *Proceedings of the IEEE conference on computer vision and pattern recognition*, pages 586–595, 2018. 6

Appendix of Adams Bashforth Moulton Solver for Inversion and Editing in Rectified Flow

(Supplementary Material)

A. More Experiment Results

A.1. User Study

To further evaluate the effectiveness of our method, we conducted a comprehensive user study. We considered several editing modalities, namely Change Material, Change Background, Change Style, Change Color, Change Pose, Change Content, Delete Object, Add Object, Change Object, and Random. For each modality, we presented two sub-figures: (1) focusing on Editing Quality, which was evaluated based on factors such as visual fidelity, sharpness of the edited regions, and how well the changes adhered to the user’s intended prompt; and (2) addressing Consistency, which measured the overall coherence of the edited image with respect to the original, including aspects like color harmony, object placement, and semantic context. Participants were asked to rate the results of our method and several baseline methods on a scale from 1 to 5 for each of these dimensions. The aggregated results, as shown in Figure 6, clearly indicate that our approach outperforms the competitors in most editing modalities. In particular, for complex edits like Change Content and Add Object, our method received significantly higher ratings in both Editing Quality and Consistency, demonstrating its superiority in handling challenging editing tasks while maintaining a high level of user satisfaction.

A.2. Comparison

To further validate the effectiveness of the ABM-Solver, we present additional experimental results in Figure 7, comparing it to other image and video editing methods. These results reinforce our earlier findings, demonstrating that ABM-Solver provides superior performance in preserving non-edited regions while achieving high-quality, semantically consistent edits. In particular, the method excels in handling challenging edits, such as changing the main subject of an image or adding new objects, without introducing artifacts or inconsistencies. Moreover, global changes like style transfer are successfully applied with minimal disruption to the original content.

In contrast, baseline methods, such as P2P, Pix2Pix-Zero, MasaCtrl, and PnP, often produce unsatisfactory edits in certain areas, as seen in the additional visual comparisons. These methods struggle with maintaining the integrity of the original image in regions that should remain unchanged. While rectified flow-based models like RF-Inversion and RF-Solver perform better than the aforementioned methods, they still exhibit minor inconsistencies, particularly in preserving the original content and in areas

requiring precise adjustments.

The ABM-Solver, however, consistently provides a more reliable and robust solution, offering better control over both the preservation of original content and the fidelity of the applied edits.

A.3. Adaptive Step Size Adjustment

In this experiment, we evaluate the effect of varying error tolerance ϵ values in the ASSA module, which controls the step size and, consequently, the trade-off between computational efficiency and precision. We conduct qualitative assessments for ϵ values ranging from 1×10^{-1} to 1×10^{-4} , with the default value being 1×10^{-1} .

The results demonstrate a clear trend: as the ϵ value increases (i.e., allowing for larger error tolerance) in Figure 8, the step size increases, leading to faster progress through the process. However, this comes at the cost of greater approximation errors, which are visible in the reconstructed images and edits. Specifically, higher ϵ values result in noticeable artifacts, such as blurriness in the edited regions, misalignment of objects, and inconsistencies in color harmony. This degradation in performance is most apparent in the complex editing tasks, where precision is crucial for maintaining the fidelity of both the original content and the desired modifications.

On the other hand, as the ϵ value decreases (i.e., tighter error tolerance), the step size becomes smaller, leading to slower but more precise processing. While this results in more accurate reconstructions and edits, it requires more computational resources, making the process slower overall.

In terms of the ASSA mechanism, we introduce an important operational detail: the error tolerance adjustment does not affect the step size during the first 5 steps and the last 5 steps of the process. This is done to maintain stable initial and final stages of the computation. During these steps, the method ensures that the step size aligns with the original second-order ABM solver, preserving consistency with the initial numerical solver.

Additionally, the minimum step size is set to be consistent with the second-order ABM sampling, ensuring that no steps are too small to cause unnecessary computational overhead. The maximum allowable step size is constrained to 4 times the initial step size, ensuring that the adjustment mechanism does not excessively accelerate the process and result in larger errors. This means that, for a total of 15 steps, the theoretical number of function evaluations (NFEs) falls within the range of 40 to 60, depending on the chosen ϵ value.

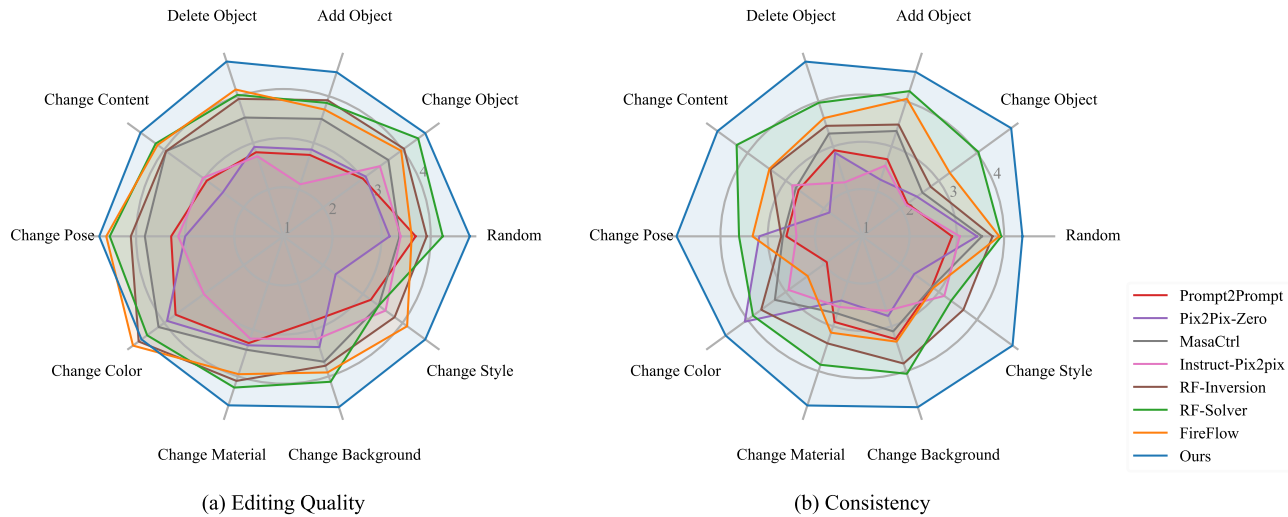


Figure 6. User study results comparing our method with several baseline approaches across various editing modalities. The study evaluates both Editing Quality (assessing visual fidelity, sharpness of the edited regions, and alignment with user prompts) and Consistency (measuring the coherence of the edited image with respect to the original, including aspects like color harmony, object placement, and semantic context). Participants (15 in total) rated the results of our method and baseline methods on a scale from 1 to 5 for each dimension.

Our experiment results reveal a trade-off between speed and accuracy. Larger ϵ values may speed up the process but at the cost of increased errors and lower editing quality. Conversely, smaller ϵ values equate to a more precise method but at the cost of computational efficiency, often resulting in a process that is closer to the original second-order ABM method without utilizing the ASSA step adjustment

B. Additional Visual Results

B.1. Image Editing

It demonstrates the effectiveness of our method in semantic image editing and stylization tasks in Figure 9. The images show how our approach preserves the core structure and content of the reference image while enabling modifications as specified by the input prompts. Notably, when content is added [+], the existing structure remains intact without undesired alterations. When content is changed [C], our model carefully adjusts the relevant regions, ensuring that the edits are both natural and semantically consistent with the original image. Style editing [S] also reveals the model’s ability to modify the overall style of the image while preserving the underlying content. This illustrates the high fidelity and flexibility of our approach in various semantic editing scenarios.

We present a set of input images with various edits applied to different attributes in Figure 10. Each row represents an input image with modifications made to specific elements, such as changes in the appearance of the human

face, object replacement the visual style of the image. Our method ensures that while individual attributes are changed, the underlying coherence of the image remains intact, maintaining the spatial and semantic integrity of the original image. This capability is essential for achieving high-quality, context-aware image editing.

As shown in Figure 11, there are a series of input images where sequential editing operations are applied, combining various content, background, and style changes. The images demonstrate how our model can handle multiple successive edits while preserving the integrity of previous modifications. This sequential compositional editing ability is vital for more complex tasks, where multiple layers of changes need to be made while maintaining consistency and avoiding artifacts. The results highlight the robustness and versatility of our method, offering significant flexibility for more intricate image editing tasks.

B.2. Image Reconstruction

We present the qualitative results of image reconstruction. We compare our method with Vallina, RF-Solver, and FireFlow in Figure 12. The visualizations include the reconstructed images, Diff maps (showing the pixel-wise differences between the original and reconstructed images), and Diff maps in the frequency domain space (providing insights into the differences in spectral characteristics). As can be seen, our approach consistently achieves higher fidelity reconstructions, with noticeably reduced differences in both the spatial and frequency domains compared to the other methods.

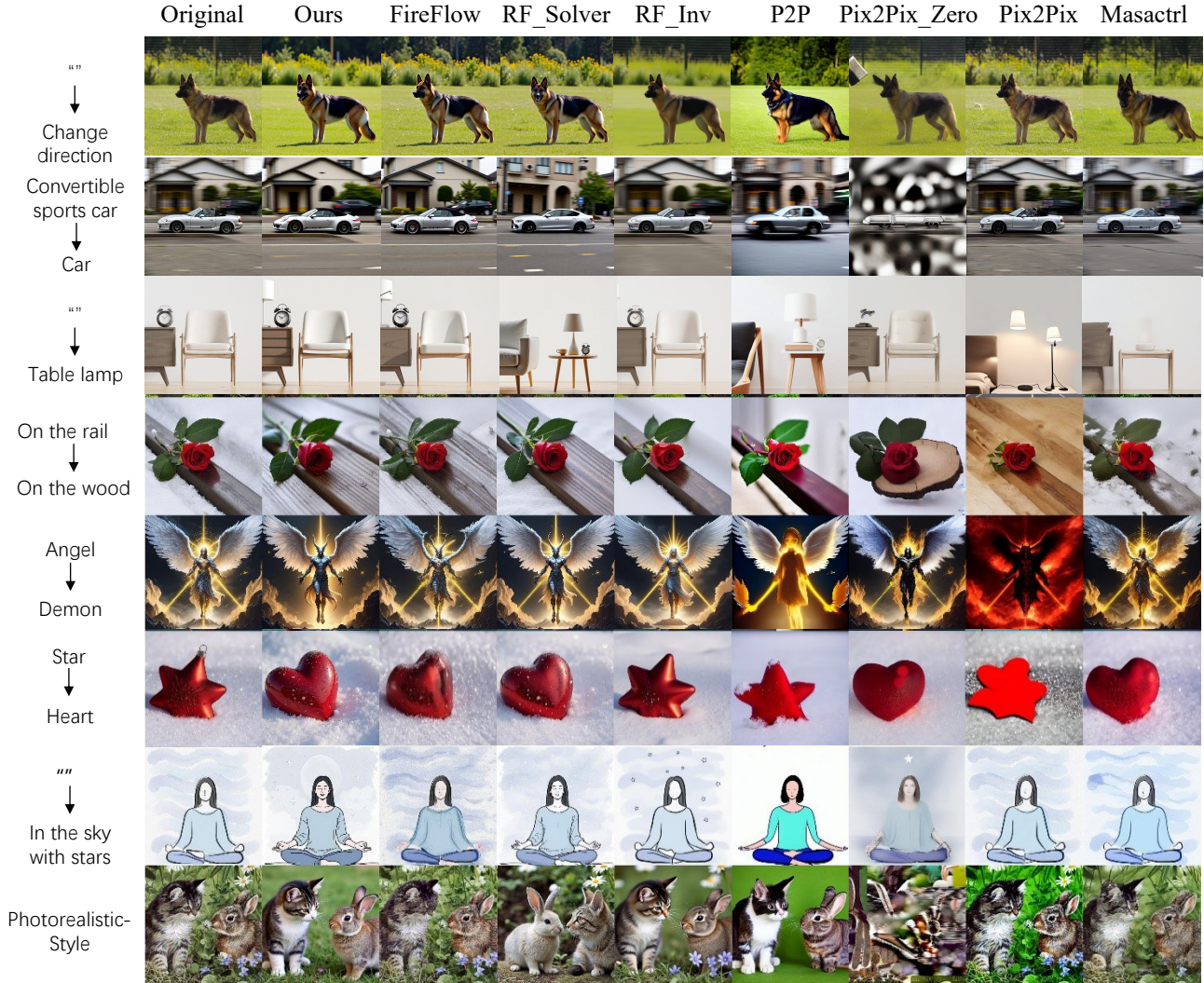


Figure 7. Qualitative comparison of image editing.

C. Technical Proofs

This section provides detailed technical proofs for the theoretical results discussed in the main text. We focus on three core aspects of the second-order Adams-Bashforth-Moulton (ABM) solver: (1) the derivation of the predictor/corrector coefficients; (2) the local and global error analysis; and (3) the preservation of convergence order under adaptive step size.

C.1. Proof 1: Derivation of the Second-Order ABM Coefficients

Outline of the Derivation. We illustrate how the standard two-step Adams-Bashforth and two-step Adams-Moulton coefficients arise via polynomial interpolation. Consider the

scalar ODE

$$\frac{dZ}{dt} = f(Z(t), t).$$

Below we denote $f_i \equiv f(Z(t_i), t_i)$ and set the step size $h = t_{i+1} - t_i$.

(a) Adams-Bashforth (predictor) The two-step Adams-Bashforth method approximates

$$\int_{t_i}^{t_{i+1}} f(Z(t), t) dt$$

Define a first-order polynomial $P_1(\tau)$ that interpolates

$$P_1(t_{i-1}) = f_{i-1}, \quad P_1(t_i) = f_i.$$

Step (1): Construct the interpolating polynomial. A lin-

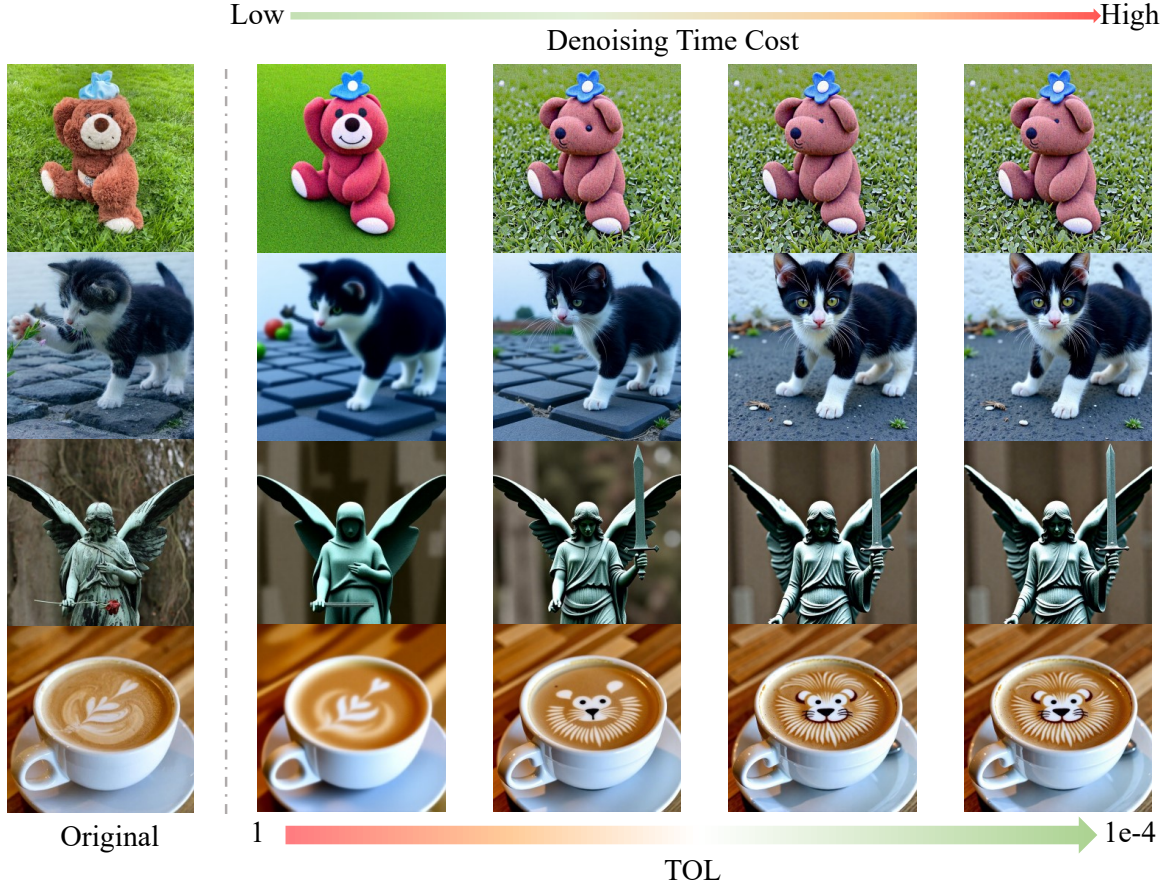


Figure 8. Qualitative results of the error tolerance ϵ experiment for the ASSA module.

ear polynomial can be expressed in the Lagrange form as

$$P_1(\tau) = f_{i-1} \cdot \frac{\tau - t_i}{t_{i-1} - t_i} + f_i \cdot \frac{\tau - t_{i-1}}{t_i - t_{i-1}}.$$

Step (2): Integrate $P_1(\tau)$ from $\tau = t_i$ to $\tau = t_{i+1}$. We want

$$\int_{t_i}^{t_{i+1}} P_1(\tau) d\tau.$$

Make a change of variable $x = \tau - t_i$. Then when $\tau = t_i$, $x = 0$; and when $\tau = t_{i+1}$, $x = h$. Hence:

$$\int_{t_i}^{t_{i+1}} P_1(\tau) d\tau = \int_0^h P_1(t_i + x) dx.$$

Hence

$$\begin{aligned} \int_0^h P_1(t_i + x) dx &= \int_0^h \left[-\frac{f_{i-1}}{h} x + \frac{f_i}{h} (x + h) \right] dx \\ &= \int_0^h \left[-\frac{f_{i-1}}{h} x + \frac{f_i}{h} x + f_i \right] dx \\ &= \int_0^h \left[\frac{f_i - f_{i-1}}{h} x + f_i \right] dx. \end{aligned}$$

Compute the integral term by term:

$$\begin{aligned} \int_0^h \frac{f_i - f_{i-1}}{h} x dx &= \frac{f_i - f_{i-1}}{h} \left[\frac{x^2}{2} \right]_0^h \\ &= \frac{f_i - f_{i-1}}{h} \frac{h^2}{2} \\ &= \frac{h}{2} (f_i - f_{i-1}), \end{aligned}$$

$$\int_0^h f_i dx = f_i [x]_0^h = f_i h.$$

Summing them:

$$\int_{t_i}^{t_{i+1}} P_1(\tau) d\tau = \frac{h}{2} (f_i - f_{i-1}) + f_i h = \frac{h}{2} (3f_i - f_{i-1}).$$

Therefore, the **two-step Adams-Bashforth approximation** to the integral is

$$\int_{t_i}^{t_{i+1}} f(\tau) d\tau \approx \frac{h}{2} [3f_i - f_{i-1}].$$

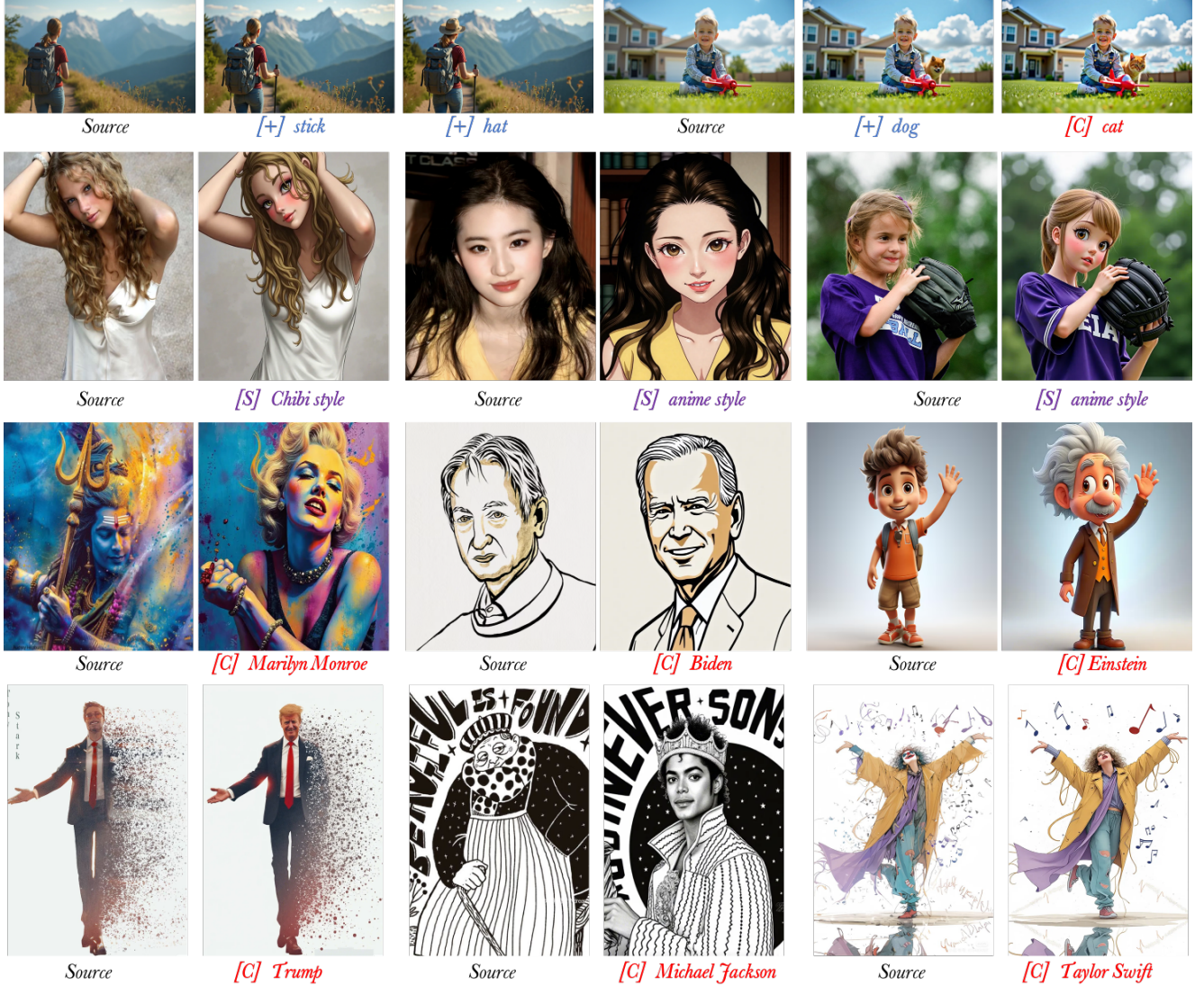


Figure 9. Our approach achieves outstanding results in semantic image editing and stylization guided by prompts, while maintaining the integrity of the reference content image and avoiding undesired alterations. [+] means adding contents, [C] indicates changes in content and [S] denotes style editing.

Recalling that the ODE update is $Z_{t_{i+1}}^{(p)} = Z_{t_i} + \int_{t_i}^{t_{i+1}} f(\tau) d\tau$, we obtain the second-order Adams-Bashforth predictor:

$$Z_{t_{i+1}}^{(p)} = Z_{t_i} + \frac{h}{2} [3f_i - f_{i-1}].$$

(b) Adams-Moulton (corrector) After obtaining the predictor $Z_{t_{i+1}}^{(p)}$, the two-step Adams-Moulton method refines the state via an integral that uses $f_{i+1} \equiv f(Z_{t_{i+1}}^{(p)}, t_{i+1})$ implicitly. The method approximates

$$\int_{t_i}^{t_{i+1}} f(Z(t), t) dt$$

Having produced a predictor $Z_{t_{i+1}}^{(p)}$, the two-step Adams-Moulton method refines the solution by incorporating the new function value $f_{i+1} = f(Z_{t_{i+1}}^{(p)})$ implicitly.

We now want to approximate the same integral

$$\int_{t_i}^{t_{i+1}} f(Z(\tau), \tau) d\tau$$

but using the values $\{f_i, f_{i+1}\}$. We construct a polynomial $Q_1(\tau)$ that interpolates (t_i, f_i) and (t_{i+1}, f_{i+1}) .

Step (1): Construct the interpolating polynomial. Again in Lagrange form,

$$Q_1(\tau) = f_i \frac{\tau - t_{i+1}}{t_i - t_{i+1}} + f_{i+1} \frac{\tau - t_i}{t_{i+1} - t_i}.$$



Figure 10. Editing different attributes of the input image, showing modifications to content and style while preserving overall image coherence.

Make a change of variable $t_{i+1} - t_i = h$. Thus

$$Q_1(\tau) = f_i \frac{\tau - (t_i + h)}{-h} + f_{i+1} \frac{\tau - t_i}{h}.$$

Step (2): Integrate $Q_1(\tau)$ from $\tau = t_i$ to $\tau = t_{i+1}$.

$$\int_{t_i}^{t_{i+1}} Q_1(\tau) d\tau.$$

Again let $x = \tau - t_i$. Then τ runs from t_i to $t_{i+1} = t_i + h$. Substituting,

$$Q_1(t_i + x) = f_i \frac{(t_i + x) - (t_i + h)}{-h} + f_{i+1} \frac{(t_i + x) - t_i}{h}.$$

Hence

$$Q_1(t_i + x) = f_i \frac{x - h}{-h} + f_{i+1} \frac{x}{h} = -\frac{f_i}{h}(x - h) + \frac{f_{i+1}}{h}x.$$

Rearrange terms:

$$Q_1(t_i + x) = -\frac{f_i}{h}x + f_i + \frac{f_{i+1}}{h}x = f_i + \frac{x}{h}(f_{i+1} - f_i).$$

Thus

$$\begin{aligned} \int_{t_i}^{t_{i+1}} Q_1(\tau) d\tau &= \int_0^h \left[f_i + \frac{x}{h}(f_{i+1} - f_i) \right] dx \\ &= \int_0^h f_i dx + \int_0^h \frac{x}{h}(f_{i+1} - f_i) dx. \end{aligned}$$

Summing,

$$\int_{t_i}^{t_{i+1}} Q_1(\tau) d\tau = f_i h + \frac{h}{2}(f_{i+1} - f_i) = \frac{h}{2}[f_{i+1} + f_i].$$

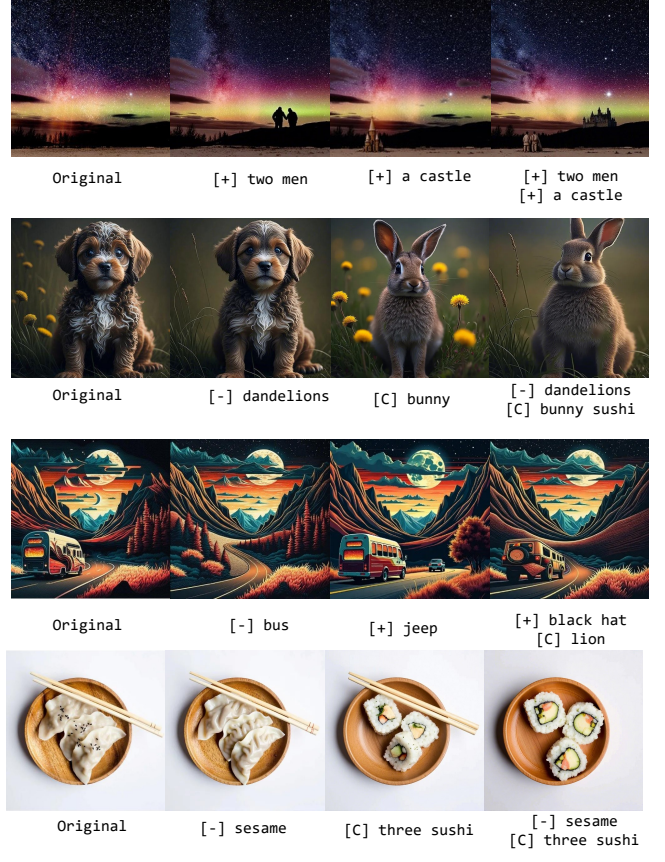


Figure 11. Sequential combination of edits applied to input images, demonstrating the flexibility of our approach in handling multiple editing tasks.

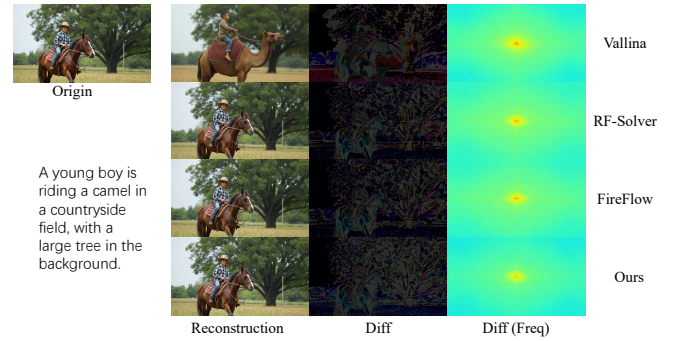


Figure 12. Qualitative results of image reconstruction comparing our method with Vanilla, RF-Solver, and FireFlow.

Thus, the two-step Adams-Moulton formula for the same integral becomes

$$\int_{t_i}^{t_{i+1}} f(\tau) d\tau \approx \frac{h}{2}[f_i + f_{i+1}].$$

Correspondingly, the corrected state update is:

$$Z_{t_{i+1}} = Z_{t_i} + \frac{h}{2} [f_{i+1} + f_i].$$

Because $f_{i+1} = f(Z_{t_{i+1}})$ depends on the unknown $Z_{t_{i+1}}$, one typically uses the predictor $Z_{t_{i+1}}^{(p)}$ to evaluate f_{i+1} . This one extra evaluation refines the estimate and achieves second-order accuracy. \square

C.2. Proof 2: Error Analysis of the Second-Order ABM Method

Sketch of the Local and Global Error Bounds. Again consider the ODE

$$\frac{dZ}{dt} = f(Z, t), \quad Z(0) = Z_0,$$

on a time interval $t \in [0, T]$. Let $h = \max_i(t_{i+1} - t_i)$ denote the largest step size. We show that the local truncation error is $\mathcal{O}(h^3)$, which in turn implies a global error $\mathcal{O}(h^2)$.

(a) Local truncation error The local truncation error (LTE) measures the discrepancy if one step of the ABM update is applied using exact solution values at the previous steps. For the two-step Adams-Bashforth predictor, one can expand $f(Z(t), t)$ in Taylor series about t_i , while for the Adams-Moulton corrector, a similar expansion centers on the interval $[t_i, t_{i+1}]$. Standard polynomial interpolation arguments (or standard texts in numerical analysis) show that for sufficiently smooth f :

$$\text{LTE}_{\text{ABM}} = \mathcal{O}(h^3).$$

(b) Global error By consistency and stability arguments (via, e.g., a discrete Grönwall lemma), the $\mathcal{O}(h^3)$ local error guarantees that the global accumulated error remains $\mathcal{O}(h^2)$ over the full interval $[0, T]$. Formally, let $Z(t)$ be the exact solution and $Z_{t_i}^{(\text{ABM})}$ the numerical solution at discrete steps. Then there exists a constant C' (independent of h) such that

$$\max_i \|Z(t_i) - Z_{t_i}^{(\text{ABM})}\| \leq C' h^2,$$

provided f is sufficiently smooth and Lipschitz continuous in Z .

Thus, the second-order ABM solver enjoys $\mathcal{O}(h^3)$ local truncation error and $\mathcal{O}(h^2)$ global convergence, as stated in the main text. \square

C.3. Proof 3: Adaptive Step Size Preserves the Convergence Order

Key Idea. Let $\{t_0, t_1, \dots, t_N\}$ be nonuniform points in $[0, T]$ determined by an adaptive step size strategy. Denote

$h_i = t_{i+1} - t_i$ and $h_{\max} = \max_i h_i$. The method's local error control (involving a tolerance ε) ensures that each individual step's local truncation error satisfies

$$\|\text{LTE}_i\| \leq K h_i^{p+1},$$

for some constant K and method order $p = 2$. Whenever the error estimate E_{i+1} in (14) exceeds the threshold ε , the step is rejected and h_i is decreased (see (15)). Conversely, if E_{i+1} is well below ε , one may increase h_i .

Because each successful step i still adheres to

$$\|\text{LTE}_i\| \leq C h_i^3, \quad (p = 2),$$

the standard global convergence argument remains valid on each subinterval $[t_i, t_{i+1}]$. As long as $h_{\max} \rightarrow 0$ with $N \rightarrow \infty$, the global error bound on $[0, T]$ follows the same $\mathcal{O}(h_{\max}^2)$ rate as in the uniform-step case. Informally:

$$\max_{0 \leq i \leq N} \|Z(t_i) - Z_{t_i}^{(\text{ABM})}\| \leq C' (h_{\max})^2,$$

where C' depends on the Lipschitz constant of f and the chosen error tolerance ε , but not on h_{\max} itself. This shows that adaptive step size control, when combined with an error-estimation step consistent with the ABM scheme's order, preserves the second-order global convergence. \square